Research Article | Vol. 24, No. 18 | 5 Sep 2016 | OPTICS EXPRESS 20437

Optics EXPRESS

NIR- and SWIR-based on-orbit vicarious calibrations for satellite ocean color sensors

MENGHUA WANG,[1,*] WEI SHI,[1,2] LIDE JIANG,[1,2] AND KENNETH VOSS[3]

[1]NOAA National Environmental Satellite, Data, and Information Service, Center for Satellite Applications and Research, E/RA3, 5830 University Research Ct., College Park, Maryland 20740, USA
[2]CIRA at Colorado State University, Fort Collins, Colorado, USA
[3]Physics Department, University of Miami, Coral Gables, Florida, USA
[*]Menghua.Wang@noaa.gov

Abstract: The near-infrared (NIR) and shortwave infrared (SWIR)-based atmospheric correction algorithms are used in satellite ocean color data processing, with the SWIR-based algorithm particularly useful for turbid coastal and inland waters. In this study, we describe the NIR- and two SWIR-based on-orbit vicarious calibration approaches for satellite ocean color sensors, and compare results from these three on-orbit vicarious calibrations using satellite measurements from the Visible Infrared Imaging Radiometer Suite (VIIRS) onboard the Suomi National Polar-orbiting Partnership (SNPP). Vicarious calibration gains for VIIRS spectral bands are derived using the in situ normalized water-leaving radiance $nL_w(\lambda)$ spectra from the Marine Optical Buoy (MOBY) in waters off Hawaii. The SWIR vicarious gains are determined using VIIRS measurements from the South Pacific Gyre region, where waters are the clearest and generally stable. Specifically, vicarious gain sets for VIIRS spectral bands of 410, 443, 486, 551, and 671 nm derived from the NIR method using the NIR 745 and 862 nm bands, the SWIR method using the SWIR 1238 and 1601 nm bands, and the SWIR method using the SWIR 1238 and 2257 nm bands are (0.979954, 0.974892, 0.974685, 0.965832, 0.979042), (0.980344, 0.975344, 0.975357, 0.965531, 0.979518), and (0.980820, 0.975609, 0.975761, 0.965888, 0.978576), respectively. Thus, the NIR-based vicarious calibration gains are consistent with those from the two SWIR-based approaches with discrepancies mostly within ~0.05% from three data processing methods. In addition, the NIR vicarious gains (745 and 862 nm) derived from the two SWIR methods are (0.982065, 1.00001) and (0.981811, 1.00000), respectively, with the difference ~0.03% at the NIR 745 nm band. This is the fundamental basis for the NIR-SWIR combined atmospheric correction algorithm, which has been used to derive improved satellite ocean color products over open oceans and turbid coastal/inland waters. Therefore, a unified vicarious gain set for VIIRS bands M1–M8 and M10–M11 has been implemented in the VIIRS ocean color data processing. Using the unified vicarious gain set, VIIRS mission-long ocean color data have been successfully reprocessed using the NIR-, SWIR-, and NIR-SWIR-based atmospheric correction algorithms.

OCIS codes: (010.0010) Atmospheric and oceanic optics; (010.1285) Atmospheric correction; (010.0280) Remote sensing and sensors; (010.4450) Oceanic optics.

References and links

1. C. R. McClain, G. C. Feldman, and S. B. Hooker, "An overview of the SeaWiFS project and strategies for producing a climate research quality global ocean bio-optical time series," Deep Sea Res. Part II Top. Stud. Oceanogr. **51**(1–3), 5–42 (2004).
2. V. V. Salomonson, W. L. Barnes, P. W. Maymon, H. E. Montgomery, and H. Ostrow, "MODIS: advanced facility instrument for studies of the Earth as a system," IEEE Trans. Geosci. Remote Sens. **27**(2), 145–153 (1989).
3. W. E. Esaias, M. R. Abbott, I. Barton, O. B. Brown, J. W. Campbell, K. L. Carder, D. K. Clark, R. L. Evans, F. E. Hodge, H. R. Gordon, W. P. Balch, R. Letelier, and P. J. Minnet, "An overview of MODIS capabilities for ocean science observations," IEEE Trans. Geosci. Remote Sens. **36**(4), 1250–1265 (1998).
4. M. Rast, J. L. Bezy, and S. Bruzzi, "The ESA Medium Resolution Imaging Spectrometer MERIS a review of the instrument and its mission," Int. J. Remote Sens. **20**(9), 1681–1702 (1999).

#270503 http://dx.doi.org/10.1364/OE.24.020437
Journal © 2016 Received 14 Jul 2016; revised 18 Aug 2016; accepted 22 Aug 2016; published 26 Aug 2016

Optics EXPRESS

5. M. D. Goldberg, H. Kilcoyne, H. Cikanek, and A. Mehta, "Joint Polar Satellite System: The United States next generation civilian polar-orbiting environmental satellite system," J. Geophys. Res. Atmos. **118**(24), 13463–13475 (2013).
6. M. Wang, X. Liu, L. Tan, L. Jiang, S. Son, W. Shi, K. Rausch, and K. Voss, "Impact of VIIRS SDR performance on ocean color products," J. Geophys. Res. Atmos. **118**(18), 10347–10360 (2013).
7. G. Thuillier, M. Herse, D. Labs, T. Foujols, W. Peetermans, D. Gillotay, P. C. Simon, and H. Mandel, "The solar spectral irradiance from 200 to 2400 nm as measured by the SOLSPEC spectrometer from the ATLAS and EURECA missions," Sol. Phys. **214**(1), 1–22 (2003).
8. H. R. Gordon and M. Wang, "Retrieval of water-leaving radiance and aerosol optical thickness over the oceans with SeaWiFS: A preliminary algorithm," Appl. Opt. **33**(3), 443–452 (1994).
9. M. Wang, "Remote sensing of the ocean contributions from ultraviolet to near-infrared using the shortwave infrared bands: simulations," Appl. Opt. **46**(9), 1535–1547 (2007).
10. IOCCG, *Atmospheric Correction for Remotely-Sensed Ocean-Colour Products*, M. Wang (Ed.), Reports of International Ocean-Color Coordinating Group, No. 10, IOCCG, Dartmouth, Canada (2010).
11. IOCCG, *Mission Requirements for Future Ocean-Colour Sensors,* C. R. McClain and G. Meister eds., Reports of International Ocean-Color Coordinating Group, No. 13, IOCCG, Dartmouth, Canada (2012).
12. H. R. Gordon, J. W. Brown, and R. H. Evans, "Exact Rayleigh scattering calculations for use with the Nimbus-7 Coastal Zone Color Scanner," Appl. Opt. **27**(5), 862–871 (1988).
13. H. R. Gordon and M. Wang, "Surface-roughness considerations for atmospheric correction of ocean color sensors. 1: The Rayleigh-scattering component," Appl. Opt. **31**(21), 4247–4260 (1992).
14. M. Wang, "A refinement for the Rayleigh radiance computation with variation of the atmospheric pressure," Int. J. Remote Sens. **26**(24), 5651–5663 (2005).
15. M. Wang, "Rayleigh radiance computations for satellite remote sensing: Accounting for the effect of sensor spectral response function," Opt. Express **24**(11), 12414–12429 (2016).
16. H. R. Gordon, "Atmospheric correction of ocean color imagery in the Earth Observing System era," J. Geophys. Res. **102**(D14), 17081–17106 (1997).
17. M. Wang, K. D. Knobelspiesse, and C. R. McClain, "Study of the Sea-Viewing Wide Field-of-View Sensor (SeaWiFS) aerosol optical property data over ocean in combination with the ocean color products," J. Geophys. Res. **110**(D10), D10S06 (2005).
18. P. Y. Deschamps, M. Herman, and D. Tanre, "Modeling of the atmospheric effects and its application to the remote sensing of ocean color," Appl. Opt. **22**(23), 3751–3758 (1983).
19. H. R. Gordon and M. Wang, "Influence of oceanic whitecaps on atmospheric correction of ocean-color sensors," Appl. Opt. **33**(33), 7754–7763 (1994).
20. R. Frouin, M. Schwindling, and P. Y. Deschamps, "Spectral reflectance of sea foam in the visible and near infrared: In situ measurements and remote sensing implications," J. Geophys. Res. **101**(C6), 14361–14371 (1996).
21. K. D. Moore, K. J. Voss, and H. R. Gordon, "Spectral reflectance of whitecaps: Their contribution to water-leaving radiance," J. Geophys. Res. **105**(C3), 6493–6499 (2000).
22. M. Wang and S. W. Bailey, "Correction of the sun glint contamination on the SeaWiFS ocean and atmosphere products," Appl. Opt. **40**(27), 4790–4798 (2001).
23. H. Zhang and M. Wang, "Evaluation of sun glint models using MODIS measurements," J. Quant. Spectrosc. Radiat. Transf. **111**(3), 492–506 (2010).
24. A. Morel and B. Gentili, "Diffuse reflectance of oceanic waters. III. Implication of bidirectionality for the remote-sensing problem," Appl. Opt. **35**(24), 4850–4862 (1996).
25. H. R. Gordon, "Normalized water-leaving radiance: revisiting the influence of surface roughness," Appl. Opt. **44**(2), 241–248 (2005).
26. M. Wang, "Effects of ocean surface reflectance variation with solar elevation on normalized water-leaving radiance," Appl. Opt. **45**(17), 4122–4128 (2006).
27. H. Yang and H. R. Gordon, "Remote sensing of ocean color: assessment of water-leaving radiance bidirectional effects on atmospheric diffuse transmittance," Appl. Opt. **36**(30), 7887–7897 (1997).
28. J. E. O'Reilly, S. Maritorena, B. G. Mitchell, D. A. Siegel, K. L. Carder, S. A. Garver, M. Kahru, and C. R. McClain, "Ocean color chlorophyll algorithms for SeaWiFS," J. Geophys. Res. **103**(C11), 24937–24953 (1998).
29. C. Hu, Z. Lee, and B. A. Franz, "Chlorophyll a algorithms for oligotrophic oceans: A novel approach based on three-band reflectance difference," J. Geophys. Res. **117**(C1), C01011 (2012).
30. M. Wang and S. Son, "VIIRS-derived chlorophyll-a using the ocean color index method," Remote Sens. Environ. **182**, 141–149 (2016).
31. A. A. Gitelson, J. F. Schalles, and C. M. Hladik, "Remote chlorophyll-a retrieval in turbid, productive estuaries: Chesapeake Bay case study," Remote Sens. Environ. **109**(4), 464–472 (2007).
32. Z. P. Lee, K. Du, and R. Arnone, "A model for the diffuse attenuation coefficient of downwelling irradiance," J. Geophys. Res. **110**, C02016 (2005).
33. A. Morel, Y. Huot, B. Gentili, P. J. Werdell, S. B. Hooker, and B. A. Franz, "Examining the consistency of products derived from various ocean color sensors in open ocean (Case 1) waters in the perspective of a multi-sensor approach," Remote Sens. Environ. **111**(1), 69–88 (2007).
34. M. Wang, S. Son, and J. L. W. Harding, Jr., "Retrieval of diffuse attenuation coefficient in the Chesapeake Bay and turbid ocean regions for satellite ocean color applications," J. Geophys. Res. **114**(C10), C10011 (2009).

Optics EXPRESS

35. S. Son and M. Wang, "Diffuse attenuation coefficient of the photosynthetically available radiation Kd(PAR) for global open ocean and coastal waters," Remote Sens. Environ. **159**, 250–258 (2015).
36. C. Cao, X. Xiong, S. Blonski, Q. Liu, S. Uprety, X. Shao, Y. Bai, and F. Weng, "Suomi NPP VIIRS sensor data record verification, validation, and long-term performance monitoring," J. Geophys. Res. Atmos. **118**(20), 11664–11678 (2013).
37. X. Xiong, J. Butler, K. Chiang, B. Efremova, J. Fulbright, N. Lei, J. McIntire, H. Oudrari, J. Sun, Z. Wang, and A. Wu, "VIIRS on-orbit calibration methodology and performance," J. Geophys. Res. Atmos. **119**(9), 5065–5078 (2014).
38. J. Sun and M. Wang, "Visible infrared imaging radiometer suite solar diffuser calibration and its challenges using a solar diffuser stability monitor," Appl. Opt. **53**(36), 8571–8584 (2014).
39. J. Sun and M. Wang, "On-orbit characterization of the VIIRS solar diffuser and solar diffuser screen," Appl. Opt. **54**(2), 236–252 (2015).
40. J. Sun and M. Wang, "On-orbit calibration of visible infrared imaging radiometer suite reflective solar bands and its challenges using a solar diffuser," Appl. Opt. **54**(24), 7210–7223 (2015).
41. R. E. Eplee, Jr., K. R. Turpie, G. Meister, F. S. Patt, B. A. Franz, and S. W. Bailey, "On-orbit calibration of the Suomi national polar-orbiting partnership visible infrared imaging radiometer suite for ocean color applications," Appl. Opt. **54**(8), 1984–2006 (2015).
42. J. Sun and M. Wang, "Radiometric calibration of the VIIRS reflective solar bands with robust characterizations and hybrid calibration coefficients," Appl. Opt. **54**(31), 9331–9342 (2015).
43. M. Wang, W. Shi, L. Jiang, X. Liu, S. Son, and K. Voss, "Technique for monitoring performance of VIIRS reflective solar bands for ocean color data processing," Opt. Express **23**(11), 14446–14460 (2015).
44. H. R. Gordon, "In-orbit calibration strategy for ocean color sensors," Remote Sens. Environ. **63**(3), 265–278 (1998).
45. M. Wang and H. R. Gordon, "Calibration of ocean color scanners: How much error is acceptable in the near-infrared," Remote Sens. Environ. **82**(2–3), 497–504 (2002).
46. B. A. Franz, S. W. Bailey, P. J. Werdell, and C. R. McClain, "Sensor-independent approach to the vicarious calibration of satellite ocean color radiometry," Appl. Opt. **46**(22), 5068–5082 (2007).
47. G. Zibordi, F. Melin, K. Voss, B. C. Johnson, B. A. Franz, E. Kwiatkowska, J. P. Huot, M. Wang, and D. Antoine, "System vicarious calibration for ocean color climate change applications: Requirements for in situ data," Remote Sens. Environ. **159**, 361–369 (2015).
48. R. E. Eplee, Jr., W. D. Robinson, S. W. Bailey, D. K. Clark, P. J. Werdell, M. Wang, R. A. Barnes, and C. R. McClain, "Calibration of SeaWiFS. II. Vicarious techniques," Appl. Opt. **40**(36), 6701–6718 (2001).
49. C. R. McClain, "A decade of satellite ocean color observations," Annu. Rev. Mar. Sci. **1**(1), 19–42 (2009).
50. D. A. Siegel, M. Wang, S. Maritorena, and W. Robinson, "Atmospheric correction of satellite ocean color imagery: the black pixel assumption," Appl. Opt. **39**(21), 3582–3591 (2000).
51. K. G. Ruddick, F. Ovidio, and M. Rijkeboer, "Atmospheric correction of SeaWiFS imagery for turbid coastal and inland waters," Appl. Opt. **39**(6), 897–912 (2000).
52. R. P. Stumpf, R. A. Arnone, R. W. Gould, P. M. Martinolich, and V. Ransibrahmanakul, "A partially coupled ocean-atmosphere model for retrieval of water-leaving radiance from SeaWiFS in coastal waters," (NASA Goddard Space Flight Center, Greenbelt, Maryland, 2003), pp. 51–59.
53. M. Wang and W. Shi, "Estimation of ocean contribution at the MODIS near-infrared wavelengths along the east coast of the U.S.: Two case studies," Geophys. Res. Lett. **32**(13), L13606 (2005).
54. G. M. Hale and M. R. Querry, "Optical constants of water in the 200nm to 200μm wavelength region," Appl. Opt. **12**(3), 555–563 (1973).
55. M. Wang and W. Shi, "The NIR-SWIR combined atmospheric correction approach for MODIS ocean color data processing," Opt. Express **15**(24), 15722–15733 (2007).
56. M. Wang, S. Son, and W. Shi, "Evaluation of MODIS SWIR and NIR-SWIR atmospheric correction algorithm using SeaBASS data," Remote Sens. Environ. **113**(3), 635–644 (2009).
57. M. Wang, J. Tang, and W. Shi, "MODIS-derived ocean color products along the China east coastal region," Geophys. Res. Lett. **34**(6), L06611 (2007).
58. M. Wang, W. Shi, and J. Tang, "Water property monitoring and assessment for China's inland Lake Taihu from MODIS-Aqua measurements," Remote Sens. Environ. **115**(3), 841–854 (2011).
59. W. Shi and M. Wang, "An assessment of the black ocean pixel assumption for MODIS SWIR bands," Remote Sens. Environ. **113**(8), 1587–1597 (2009).
60. D. K. Clark, H. R. Gordon, K. J. Voss, Y. Ge, W. Broenkow, and C. Trees, "Validation of atmospheric correction over the ocean," J. Geophys. Res. **102**(D14), 17209–17217 (1997).
61. M. Wang, J. H. Ahn, L. Jiang, W. Shi, S. Son, Y. J. Park, and J. H. Ryu, "Ocean color products from the Korean Geostationary Ocean Color Imager (GOCI)," Opt. Express **21**(3), 3835–3849 (2013).
62. M. Wang, "A sensitivity study of SeaWiFS atmospheric correction algorithm: Effects of spectral band variations," Remote Sens. Environ. **67**(3), 348–359 (1999).
63. M. Wang and B. A. Franz, "Comparing the ocean color measurements between MOS and SeaWiFS: A vicarious intercalibration approach for MOS," IEEE Trans. Geosci. Remote Sens. **38**(1), 184–197 (2000).
64. M. Wang, A. Isaacman, B. A. Franz, and C. R. McClain, "Ocean-color optical property data derived from the Japanese ocean color and temperature scanner and the french polarization and directionality of the earth's reflectances: a comparison study," Appl. Opt. **41**(6), 974–990 (2002).

Optics EXPRESS

65. E. P. Shettle and R. W. Fenn, "Models for the aerosols of the lower atmosphere and the effects of humidity variations on their optical properties," (U.S. Air Force Geophysics Laboratory, Hanscom Air Force Base, Mass., 1979), pp. 1–94.
66. M. Wang, X. Liu, L. Jiang, S. Son, J. Sun, W. Shi, L. Tan, P. Naik, K. Mikelsons, X. Wang, and V. Lance, "Evaluation of VIIRS ocean color products," Proc. SPIE **9261**, 92610E (2014).
67. M. Wang and W. Shi, "Sensor noise effects of the SWIR bands on MODIS-derived ocean color products," IEEE Trans. Geosci. Remote Sens. **50**(9), 3280–3292 (2012).

1. Introduction

Ocean color satellite sensors such as the Sea-viewing Wide Field-of-view Sensor (SeaWiFS) [1], the Moderate Resolution Imaging Spectroradiometer (MODIS) on the Terra and Aqua satellites [2, 3], the Medium Resolution Imaging Spectrometer (MERIS) on the Envisat [4], and the Visible Infrared Imaging Radiometer Suite (VIIRS) on the Suomi National Polar-orbiting Partnership (SNPP) [5, 6] measure the top-of-atmosphere (TOA) radiance $L_t(\lambda)$ or reflectance $\rho_t(\lambda)$, where $\rho_t(\lambda) = \pi\, L_t(\lambda) / [F_0(\lambda) \cos\theta_0]$ with $F_0(\lambda)$ as the extraterrestrial solar irradiance [7] and θ_0 as the solar-zenith angle, at multiple wavelengths from the visible to the near-infrared (NIR) and shortwave infrared (SWIR), which are designed for satellite ocean color remote sensing [8–11]. For the ocean-atmosphere system, the satellite sensor-measured TOA radiances can be expressed as [8–10]:

$$L_t(\lambda) = L_r(\lambda) + L_A(\lambda) + t(\lambda) L_{wc}(\lambda) + T(\lambda) L_g(\lambda) + t(\lambda) t_0(\lambda) \cos\theta_0\, nL_w(\lambda), \quad (1)$$

where $L_r(\lambda)$ and $L_A(\lambda)$ are radiance contributions from scattering by air molecules (Rayleigh scattering) [12–15] and aerosols (including multiple Rayleigh-aerosol interactions) [8, 16–18], respectively. $L_{wc}(\lambda)$ and $L_g(\lambda)$ are the radiance components due to sea surface whitecaps [19–21] and the surface specular reflection of direct sunlight (sun glitter) [22, 23], respectively, and $nL_w(\lambda)$ is the normalized water-leaving radiance due to photons that penetrate the sea surface and are backscattered out of the water [10, 24–26]. The quantities $t_0(\lambda)$ and $t(\lambda)$ are the atmospheric diffuse transmittances [10, 27] from the sun (with solar-zenith angle of θ_0) to the water surface and from the water surface to the sensor (with sensor-zenith angle of θ), respectively. The parameter $T(\lambda)$ is the direct atmospheric transmittance (with sensor-zenith angle of θ) from the water surface to the sensor [22]. To be brief, in this discussion it is assumed that the gas absorption effect has been accounted for in Eq. (1).

Because the atmosphere and ocean surface radiance contributions (first four terms in Eq. (1)) can account for more than ~90% of the TOA radiance in the visible wavelengths [8–10], satellite-derived ocean color products such as normalized water-leaving radiance spectra $nL_w(\lambda)$ [8, 10], chlorophyll-a (Chl-a) concentration [28–31], water diffuse attenuation coefficient at the wavelength of 490 nm $K_d(490)$ (or at photosynthetically available radiation (PAR) between 400 and 700 nm K_d(PAR)) [32–35], etc., are highly sensitive to the performance of the satellite sensor on-orbit calibration [36–42]. This places highly stringent requirements on the sensor on-orbit radiometric calibration for ocean color remote sensing, in particular, for the short visible bands. Even for a perfect atmospheric correction [8–10], i.e., effects of the atmosphere and ocean surface are accurately removed (first four terms in Eq. (1)), the error in the satellite-derived $nL_w(\lambda)$ spectra will be at least 10 times of the error in the sensor calibration (the ten-to-one rule). Thus, the uncertainty of ~0.1% in the sensor radiometric calibration leads to ~1% (or more) in the satellite-measured $nL_w(\lambda)$ at the short visible bands for open oceans [43]. To meet the accuracy of ~30% in satellite-measured Chl-a in the open ocean, it requires an uncertainty less than ~5% for the satellite-derived $nL_w(\lambda)$ in the blue bands [8, 10], i.e., the sensor on-orbit calibration should be at least within ~0.5%. Therefore, in addition to accurately tracking the sensor degradation using the solar and lunar methods [36–40, 42], the key calibration procedure for satellite ocean color remote sensing is the on-orbit vicarious calibration (VC) [44–47]. This procedure accounts for all of the components of the TOA radiances reflected from the ocean-atmosphere system by direct measurements or by calculations (simulations) based on in situ measurements and radiative

Optics EXPRESS

transfer theory. The calculated/simulated TOA radiances are then compared with those from sensor measurements, and VC gains can be derived to force the measurements (from satellite) and computations into confluence with the assumption that the computed TOA radiances are the correct values.

Gordon (1998) [44] outlined a strategy for the sensor on-orbit VC for ocean color data processing. In this methodology, it is basically assumed that the longest wavelength band for ocean color data processing (e.g., the NIR 865 nm for SeaWiFS) is perfectly calibrated at prelaunch (or calibrated with other methods on-orbit), and then all other bands (shorter than the longest NIR band) are effectively calibrated with respect to the longest NIR band. In fact, it is really a relative spectral VC approach [44]. For the NIR band calibration, *Wang and Gordon* (2002) [45] show that, when using the *Gordon and Wang* (1994) [8] atmospheric correction algorithm, the on-orbit VC can produce sufficiently accurate TOA radiances for ocean color data processing as long as the calibration error at the longest NIR band is within ~5% in magnitude. Importantly, this on-orbit VC approach does not depend on the sensor initial prelaunch calibration uncertainty for all the shorter wavelengths (e.g., shorter than the longest NIR band) [45], suggesting that efforts and resources should be placed on radiometric stability and complete prelaunch characterization of the instrument instead of sensor prelaunch absolute calibration. This sensor on-orbit VC methodology that uses the longest NIR band as the reference has been successfully applied to SeaWiFS, MODIS, MERIS, VIIRS, etc., for producing accurate global ocean color product data [6, 46, 48, 49].

For the NIR-based VC approach [44], the two NIR bands are used for atmospheric correction in the ocean color data processing with the assumption of a black ocean at these two NIR bands [8, 10], i.e., no $nL_w(\lambda)$ contributions at the NIR bands. However, the NIR black ocean assumption is often invalid for turbid coastal and inland waters [50–53], leading to significant errors in satellite-derived ocean color products. Based on the fact that waters are much more strongly absorbing at the SWIR bands compared with those at the NIR bands [54], the SWIR-based atmospheric correction algorithm has been proposed [9, 53, 55] and demonstrated to improve satellite ocean color products over turbid coastal and inland waters [56–58]. It has been shown that the ocean black pixel assumption is generally valid for the MODIS SWIR bands at 1240, 1640, and 2130 nm for highly turbid waters [59], and the assumption should also be valid for the three VIIRS-SNPP SWIR bands at 1238, 1601, and 2257 nm. Thus, for the SWIR-based atmospheric correction for ocean color data processing, the SWIR-based on-orbit VC has been developed and applied to the satellite ocean color data processing to improve ocean color data quality over coastal and inland waters.

In this paper, we develop and describe the NIR- and SWIR-based VC approaches for satellite ocean color data processing. In situ $nL_w(\lambda)$ data from the Marine Optical Buoy (MOBY) in waters off Hawaii [60] are used for deriving vicarious gains at the visible bands using both the NIR- and SWIR-based VC approaches for VIIRS-SNPP. The SWIR gains have been determined from the South Pacific Gyre (SPG) region where ocean waters are the clearest and generally stable. The Multi-Sensor Level-1 to Level-2 (MSL12) ocean color data processing system has been used to process satellite data as well as inversely derive vicarious gains. The VC gain sets derived from the NIR- and SWIR-based methods for VIIRS-SNPP are compared and evaluated. We show that the vicarious gains from the SWIR-based approaches are consistent with those from the NIR-based method. Thus, a consistent and unified vicarious gain set can be employed for satellite ocean color data processing using different atmospheric correction algorithms for various water cases, e.g., the NIR-based [8], the two SWIR-based [9], and the NIR-SWIR combined algorithm [55] for VIIRS global ocean color data processing.

2. Basic physics for the sensor on-orbit vicarious calibration

In the on-orbit VC for satellite ocean color sensors, the quantities of each term on the right-hand-side of Eq. (1) are estimated and summed, and the sensor calibration is adjusted to yield

Optics EXPRESS

a value of $L_t(\lambda)$ that is in agreement with the estimation. Specifically, the TOA Rayleigh-scattering radiance $L_r(\lambda)$ is computed using the solar-sensor geometry, atmospheric pressure, and surface wind speed [12–15]. Surface whitecap radiance contribution $L_{wc}(\lambda)$ is estimated using the model with wind speed input [19]. Sun glint is generally avoided [22] in VC. Aerosol radiance $L_A(\lambda)$ and atmospheric diffuse transmittance $t(\lambda)$ (or $t_0(\lambda)$) can be calculated using the radiative transfer theory with aerosol models [27]. The normalized water-leaving radiance $nL_w(\lambda)$ spectra are measured directly at the VC site, e.g., from the MOBY site in Hawaii [60]. Generally, we can write the satellite-measured TOA radiance as:

$$L_t^{(M)}(\lambda) = \left[1 + a(\lambda)\right] L_t^{(T)}(\lambda), \tag{2}$$

where $L_t^{(M)}(\lambda)$ is the radiance that would be measured by a satellite sensor and $L_t^{(T)}(\lambda)$ is the TOA "true" radiance. The quantity $a(\lambda)$ is the sensor calibration error (before the VC). After the VC, the sensor-measured TOA radiance is modified as:

$$L_t^{(C)}(\lambda) = \left[1 + a'(\lambda)\right] L_t^{(T)}(\lambda), \tag{3}$$

where $L_t^{(C)}(\lambda)$ is the "corrected" sensor-measured TOA radiance and $a'(\lambda)$ is the residual calibration error after the VC. In fact, we can also write Eq. (3) as:

$$L_t^{(C)}(\lambda) = g(\lambda)\, L_t^{(M)}(\lambda), \tag{4}$$

where $g(\lambda)$ is the derived vicarious gain coefficients from the on-orbit vicarious calibration. *Wang and Gordon* (2002) [45] show that the residual calibration error $a'(\lambda)$ in Eq. (3) depends on the quality of the VC in situ optics data (e.g., MOBY in situ data), but not on the calibration error $a(\lambda)$ for λ less than the longest wavelength in the VC spectral band (e.g., the NIR 865 nm for SeaWiFS). It is noted that, for the longest wavelength band λ_l, $a'(\lambda_l) = a(\lambda_l)$, because it is assumed that $L_t(\lambda_l)$ is error free (or calibrated with other methods) in the VC procedure [44, 45].

Figure 1 shows simulation results of the ratio $a'(\lambda)/a'(\lambda_l)$ after the VC with λ_l = 865 nm as a function of the wavelength for $a(\lambda_l)$ (or $a'(\lambda_l)$) of ± 5%, ± 10%, and ± 15%. For this demonstration, the VC has been carried out specifically for an aerosol optical thickness of 0.05 at 865 nm (i.e., $\tau_a(865) = 0.05$) with a known aerosol model (i.e., the VC has been carried out with the same aerosol model as at the VC site) and for solar-zenith angle θ_0, sensor-zenith angle θ, and relative azimuth-angle $\Delta\phi$ of 20°, 20°, and 90°, respectively. For cases with aerosol models different from that in the VC site, results are different, but quite close [45]. In addition, Fig. 1 also plots the curves of $(\lambda/\lambda_l)^4$ and $(\lambda/\lambda_l)^3$ that demonstrates a fundamental result of the VC procedure for satellite ocean color data processing—the ratio of the residual calibration error $a'(\lambda)/a'(\lambda_l)$ after the VC varies more or less according to the inverse of the Rayleigh-scattering (molecules scattering), i.e., $(\lambda/\lambda_l)^4$. Thus, results in Fig. 1 show that, using the outlined on-orbit VC scheme [44], $a'(\lambda)$ in the visible can be reduced to about an order of magnitude less than $a'(\lambda_l)$. It also shows that the *vicarious calibration should go from the longest wavelength* (i.e., at the NIR 865 nm in Fig. 1) *to the shorter wavelengths* in order to fully use the power of Rayleigh-scattering, i.e., inversely proportional to the fourth power of the wavelength. Calibration errors are enlarged significantly when the VC is carried out from the shorter wavelengths to the longer wavelengths. This is a very important point for the VC approach and further emphasized here.

Optics EXPRESS

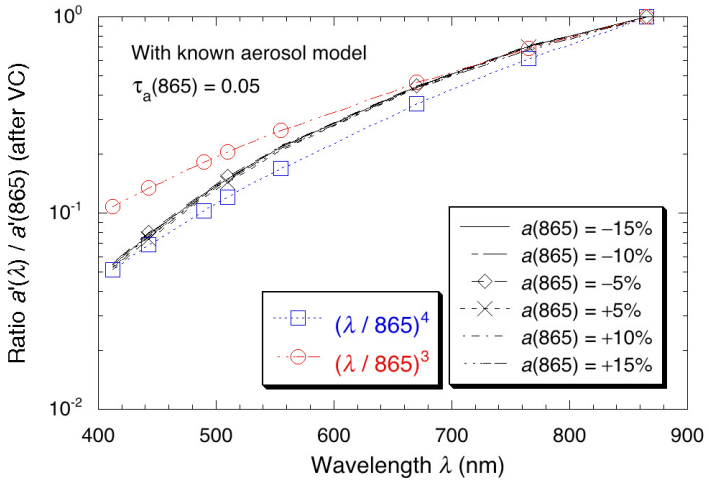

Fig. 1. Simulation results of the residual calibration error ratio $a'(\lambda)/a'(\lambda_I)$ after the VC with λ_I = 865 nm as a function of wavelength for $a(\lambda_I)$ = ± 5%, ± 10%, and ± 15%. The simulations assume a known aerosol model in the VC site with an aerosol optical thickness of 0.05 at 865 nm.

3. Methodology and data

3.1. The MSL12 ocean color data processing system

The MSL12, which is the official NOAA VIIRS ocean color data processing system, has been used for processing satellite ocean color data from Sensor Data Records (SDR) (or Level-1B) to Environmental Data Records (EDR) (or Level-2) products for VIIRS, as well as other sensors, e.g., MODIS-Aqua, the Korean Geostationary Ocean Color Imager (GOCI) [61]. MSL12 was developed for the purpose of using a consistent and common data processing system to produce ocean color data from multiple satellite ocean color sensors [62–64]. Specifically, NOAA-MSL12 is based on the SeaWiFS Data Analysis System (SeaDAS) version 4.6 with some important modifications and improvements. In particular, these improvements and updates include the SWIR-based and NIR-SWIR combined atmospheric correction algorithms for improved ocean color data products in coastal and inland waters [9, 55–58], as well as some applications related to the SWIR-based ocean color data processing.

It should be noted that 12 aerosol models are used in the MSL12. Specifically, these aerosol models are the Oceanic model with the relative humidity (RH) of 99% (O99), the Maritime model with RH of 50%, 70%, 90%, and 99% (M50, M70, M90, and M99), the Coastal model with RH of 50%, 70%, 90%, and 99% (C50, C70, C90, and C99), and the Tropospheric model with RH of 50%, 90%, and 99% (T50, T90, and T99). These aerosol models are either directly from or derived based on the *Shettle and Fenn* (1979) models [65] for satellite ocean color data processing [8–10]. In addition, as the official VIIRS ocean color data processing system, MSL12 has been used for routine production of VIIRS global ocean color products (including global daily, 8-day, monthly, and climatology images) since the VIIRS launch on October 28, 2011 [6].

There are two modes for ocean color data processing in MSL12. In the normal forward ocean color data processing mode, fixed VC gain coefficients $g(\lambda)$ are applied to satellite-measured TOA radiance $L_t^{(M)}(\lambda)$ (i.e., SDR or Level-1B data) to carry out atmospheric correction and derive ocean color products such as $nL_w(\lambda)$ spectra, Chl-a, $K_d(490)$, $K_d(\text{PAR})$, inherent optical properties (IOPs), etc. Thus, $L_t^{(C)}(\lambda)$ data from Eq. (4) are used for satellite ocean color data processing. In the MSL12 inverse data processing mode, however, in situ

Optics EXPRESS

$nL_w(\lambda)$ radiance spectra (or other known $nL_w(\lambda)$ radiance spectra) can be used as inputs to compute the nominal TOA radiances for given satellite pixels collocated at the in situ measurement location based on Eq. (1), and VC gain coefficients $g(\lambda)$ for the matchup pixels are consequently generated as the ratio between the computed TOA radiance $L_t^{(C)}(\lambda)$ and the satellite-measured radiance $L_t^{(M)}(\lambda)$ (Eq. (4)), i.e., $g(\lambda) = L_t^{(C)}(\lambda) / L_t^{(M)}(\lambda)$. It should be noted that, for both the forward and inverse data processing, ocean color data processing algorithms in MSL12 are the same (i.e., the same algorithms for both forward and inverse ocean color data processing).

3.2. MOBY in situ measurements

In situ hyperspectral radiometric data were measured at the MOBY site [60] moored off the island of Lanai in Hawaii (http://moby.mlml.calstate.edu/MOBY-data). The location of the MOBY site (20°49.0′N, 157°11.5′W) is in usually stable and clear-ocean (oligotrophic) waters. The water mass at the MOBY site is generally horizontally homogeneous, clear, and deep water, while the atmosphere over the MOBY site is predominantly marine aerosols with generally low aerosol reflectance contributions (i.e., low aerosol optical thickness) and is free of terrestrial influence. The MOBY program (currently funded by NOAA) has provided consistently high-quality clear-ocean hyperspectral optics data since 1997, supporting the VC of various satellite ocean color missions, e.g., SeaWiFS, MODIS, MERIS, VIIRS, etc. In particular, to monitor, evaluate, and assess VIIRS SDR (or Level-1B) and ocean color EDR (or Level-2) products, in situ $nL_w(\lambda)$ measurements at the VIIRS-spectrally-weighted bands from January 2012 to the present were obtained from the NOAA CoastWatch website (http://coastwatch.noaa.gov/moby/). In addition to the VC, it is particularly useful to evaluate the VIIRS on-orbit calibration performance and the stability of the SDR by comparing VIIRS-derived $nL_w(\lambda)$ with those from MOBY in situ measurements [6, 43, 66]. For this study, MOBY in situ optics data are used as input for running MSL12 (inverse mode) to derive the VC gains $g(\lambda)$ for VIIRS-SNPP using both the NIR- and SWIR-based VC approaches.

3.3. The NIR- and SWIR-based VC approaches

In the MSL12 ocean color data processing system, an inverse data processing module has been developed to compute the TOA radiance in the exact retrieval-reversal process for all radiance components in Eq. (1), i.e., $L_r(\lambda)$, $L_A(\lambda)$, $L_{wc}(\lambda)$, and $L_g(\lambda)$, as well as atmospheric direct and diffuse transmittances $T(\lambda)$ and $t(\lambda)$ (or $t_0(\lambda)$), corresponding to the visible, NIR, and SWIR bands. In situ measurements of $nL_w(\lambda)$ from MOBY site are used to complete the TOA radiance contribution in Eq. (1). The MOBY observation closest in time to the satellite overpass is chosen from the three daily MOBY measurements, and normally these are observations at ~00:00 UTC. The matchup pixel is identified in the corresponding VIIRS images. An 11 × 11 pixel box centered at the MOBY matchup pixel is used for further screening and quality control of satellite observations, and computing the VC gains. The data screening criteria include an aerosol optical thickness at the NIR band (e.g., VIIRS 862 nm) less than 0.15, a sun glint coefficient [22] less than 0.005, solar- and sensor-zenith angles θ_0 and θ less than 70° and 55°, respectively, and no associated flags such as clouds, stray light or atmospheric correction failure. If a pixel passes the above criteria, matchup in situ MOBY $nL_w(\lambda)$ data are used to compute the TOA radiance $L_t^{(C)}(\lambda)$, and VC gains are then derived according to Eq. (4). In this work, MOBY in situ measurements between February 2012 and April 2016 are used to find VIIRS-MOBY matchups for the on-orbit VC for VIIRS-SNPP.

As discussed, the same retrieval-reversal data processing can be applied for both the NIR- and SWIR-based ocean color data processing using the MSL12. Furthermore, it is particularly noted that the VC gain coefficients for the NIR- and SWIR-based VC procedures are derived independently (separately) from the NIR- and SWIR-based ocean color data processing using

Optics EXPRESS

the MSL12. In addition, the SWIR-based vicarious calibration approach can derive VC gains for the visible and NIR bands, while only the visible VC gains can be derived using the NIR-based VC method. Specifically, for VIIRS-SNPP, the two NIR bands at 745 and 862 nm (M6 and M7) are used for the NIR-based VC [8], while the SWIR bands at 1238 and 1601 nm (M8 and M10) (named SWIR1) and the SWIR bands at 1238 and 2257 nm (M8 and M11) (named SWIR2) are employed for the SWIR-based VC approaches [9]. Therefore, VIIRS global ocean color data products can be derived using the NIR-, SWIR1-, and SWIR2-based, as well as the NIR-SWIR combined, ocean color data processing using the MSL12.

3.4. Specific VC procedure for VIIRS

Some extensive tests and evaluations have been carried out in order to develop robust VC approaches (i.e., detailed procedures and steps) for VIIRS-SNPP. In fact, we have developed the VC procedure for VIIRS using MOBY in situ optics data and VIIRS observations at the SPG and Hawaii MOBY ocean regions to derive VC gains $g(\lambda)$ for the VIIRS visible, NIR, and SWIR spectral bands. The specific VC procedure for VIIRS-SNPP is outlined below.

1. Set initial VC gains at the VIIRS SWIR bands 1238 nm (M8) and 1601 nm (M10) to be 1.

2. Using fixed two aerosol models M70 and M90 with equal weight (i.e., 50% for each model), the SWIR-based VC procedure can be carried out to derive the VC gain for VIIRS SWIR band M8 (1238 nm) in the SPG region. Note that the VC gain for the SWIR 1601 nm band is still 1 at the first iteration.

3. Using the derived VC gains at the SWIR 1238 and 1601 nm bands from the SPG region, the SWIR-based ocean color data processing can be carried out to derive VC gains for the VIIRS two NIR bands 745 and 862 nm (M6 and M7) at the MOBY site. This process assumes the black ocean pixel (i.e., $nL_w(\lambda) = 0$) in Eq. (1) for the VIIRS two NIR bands at the MOBY site.

4. Iterate steps 2–3, adjusting of the VC gains at the VIIRS 1238 and 1601 nm bands at the SPG site until the derived gain at the NIR 862 nm band is 1. Specifically, if the NIR 862 nm gain is smaller (or larger) than 1, the gain of the SWIR 1601 nm band is then increased (or decreased) and the SPG procedure (step 2) is re-run to derive the gain for the SWIR 1238 nm band. The step 3 is carried out to re-derive the NIR 862 nm gain. The iteration is continued until the gain for the NIR 862 nm band is converged to 1. Thus, VC gains for the two NIR bands are derived with the goal to have the VIIRS 862 nm band equal to 1. This is due to the fact that VIIRS on-orbit radiometric calibration for the NIR bands is more accurate and reliable than those of the SWIR bands (i.e., we have more confidence with the accuracy of the NIR calibrations than those of the SWIR bands). At the same time, the VC gains for all visible bands (M1–M5) can be derived using the SWIR-based data processing with the VIIRS SWIR bands 1238 and 1601 nm. Thus, VC gains for VIIRS visible and NIR bands are derived using the SWIR1-based data processing (i.e., using the two SWIR bands at 1238 and 1601 nm).

5. With the derived two NIR VC gains, the NIR-based ocean color data processing (inverse processing in the MSL12) can be carried out to derive VC gains for all visible bands M1–M5. It is noted that, except for the VC gains at the two NIR bands, the SWIR1-derived and NIR-derived VC gains at the VIIRS visible bands (M1–M5) are independently derived using the MSL12.

6. Repeat step 4 to adjust the VIIRS SWIR band at 2257 nm using the SWIR band at 1238 nm (with the VC gain derived in the step 4 for the SWIR 1238 nm band) to make the gain of the VIIRS NIR 862 nm band equal to 1 at the MOBY site. Note that

Optics EXPRESS

the two SWIR bands at 1238 and 2257 nm are used for the data processing and only VC gain at the SWIR 2257 nm is adjusted (no gain changes for other two SWIR bands). Again, VC gains for the two NIR bands can be derived keeping the gain at the longest NIR band equal to 1. At the same time (once the gain at the NIR 862 nm is equal to 1), VC gains for all visible bands (M1–M5) and the NIR 745 nm (M6) can be derived. This is the SWIR2-based approach using the SWIR 1238 and 2257 nm bands for the ocean color data processing.

Therefore, three VC gain sets are derived for VIIRS ocean color data processing, i.e., VC gain sets from the NIR-based (745 and 862 nm), SWIR1-based (1238 and 1601 nm), and SWIR2-based (1238 and 2257 nm). To show results clearly, we use parameters $g^{(NIR)}(\lambda)$, $g^{(SWIR1)}(\lambda)$, and $g^{(SWIR2)}(\lambda)$ as the VC gain coefficient sets derived from these approaches.

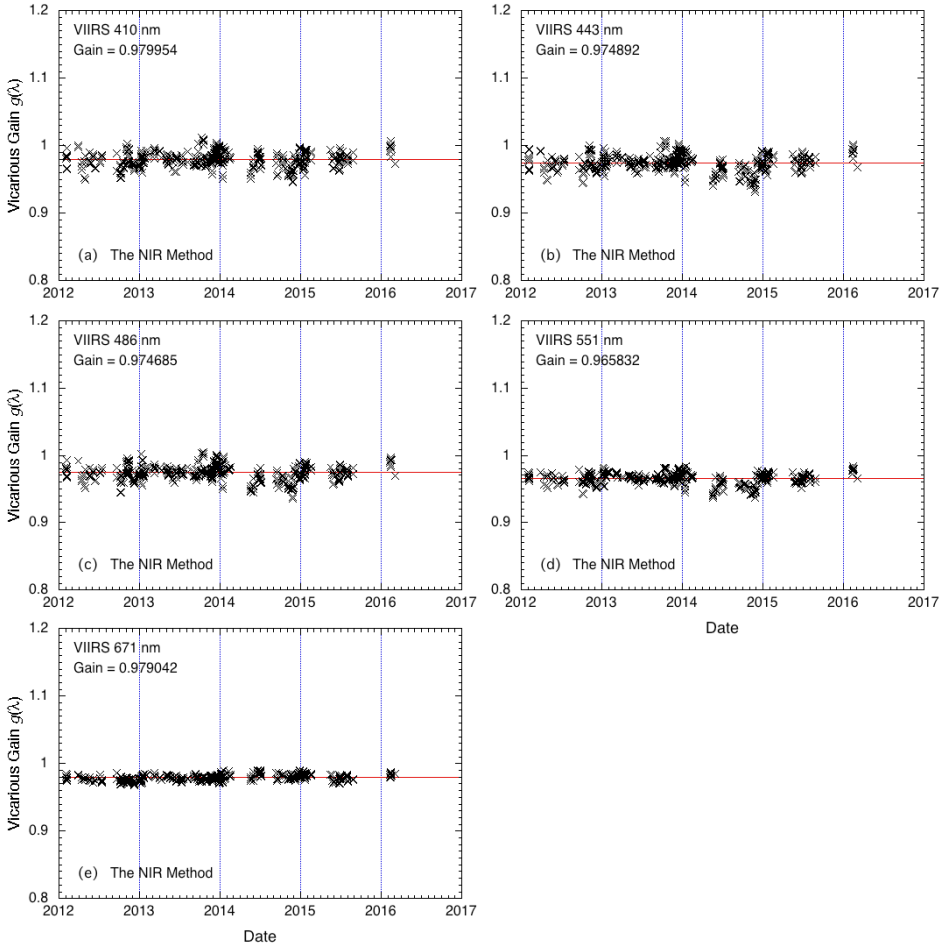

Fig. 2. VC gains $g^{(NIR)}(\lambda)$ as a function of time from 2012 to 2016 derived using the NIR-based VC method for VIIRS bands at (a) 410 nm, (b) 443 nm, (c) 486 nm, (d) 551 nm, and (e) 671 nm. For a clear demonstration, $g^{(NIR)}(\lambda)$ values are plotted in every 50 values for each plot.

Optics EXPRESS

4. Results

4.1. VIIRS-derived VC gains using the NIR-based approach

Following the procedure outlined in the previous section, the SWIR VC gains at 1238 and 1601 nm were derived at the SPG site. Through the iterations at both MOBY and SPG sites as outlined in Section 3.4, the NIR VC gains at the VIIRS 745 and 862 nm were also derived using the NIR $nL_w(\lambda) = 0$ at the MOBY site (i.e., using the black pixel assumption). The goal for the iteration is to derive the VC gain of 1 for the longest VIIRS NIR band at 862 nm. Effectively, this assumes that the on-orbit instrument radiometric calibration for the VIIRS 862 nm band is more robust and accurate than those of the SWIR bands. In fact, there are some issues with the SWIR bands calibration. After several rounds of the data processing and gain adjustments iteratively, the two NIR gains $g^{(SWIR1)}(745)$ and $g^{(SWIR1)}(862)$ converged to 0.982065 and 1.00001 when the SWIR gains $g^{(SWIR1)}(1238)$ and $g^{(SWIR1)}(1601)$ were adjusted (iteratively) to 1.01812 and 0.994676, respectively. The iteration stopped with the NIR gain $g^{(SWIR1)}(862)$ of 1.00001, which was close enough to the goal of 1.

Using the NIR gains $g^{(NIR)}(745)$ and $g^{(NIR)}(862)$ of 0.982065 and 1.0 (same values as for $g^{(SWIR1)}(745)$ and $g^{(SWIR1)}(862)$), the NIR-based VC procedure was carried out to derive $g^{(NIR)}(\lambda)$ in the visible bands following the step (5) in Section 3.4. Figure 2 shows VIIRS NIR-based VC gain $g^{(NIR)}(\lambda)$ as a function of time for $g^{(NIR)}(410)$ (Fig. 2(a)), $g^{(NIR)}(443)$ (Fig. 2(b)), $g^{(NIR)}(486)$ (Fig. 2(c)), $g^{(NIR)}(551)$ (Fig. 2(d)), and $g^{(NIR)}(671)$ (Fig. 2(e)), respectively. In Fig. 2, a subset of $g^{(NIR)}(\lambda)$ values as a function of time is plotted, once every 50 values, from total of 21891 VC gain values for each band in an 11 × 11 pixel box centered at the MOBY location. It is noted that this is pixel-based VC gain, i.e., each valid pixel has a VC gain. The median VC gains derived using the NIR-based VC approach for VIIRS bands M1–M5 are listed in Table 1. The median is used, rather than the mean, to effectively eliminate the possible effects of the outliers. The corresponding standard deviation (STD) values of the VC gains for these five VIIRS visible bands are also listed in Table 1. It is noted that the noise in terms of the $g^{(NIR)}(\lambda)$ STD performance generally trends lower from blue to red bands (Table 1), i.e., shorter to longer wavelengths (also visually observable from Fig. 2). This is due to the fact that the noise (or error) of the VC gains is largely driven by the imperfect atmospheric correction in the ocean color data processing, i.e., larger errors in the derived $nL_w(\lambda)$ at the shorter wavelengths [8].

4.2. VIIRS-derived VC gains using the SWIR1-based approach

Similar to the NIR-based VC computation as shown in Section 4.1, the box of 11 × 11 pixels centered at the MOBY location between February 2012 and April 2016 is used to compute the SWIR1-based VC gain coefficients $g^{(SWIR1)}(\lambda)$ using the VIIRS SWIR bands 1238 and 1601 nm. Figures 3(a)–3(g) show VIIRS-derived VC gain $g^{(SWIR1)}(\lambda)$ as a function of time for $g^{(SWIR1)}(410)$, $g^{(SWIR1)}(443)$, $g^{(SWIR1)}(486)$, $g^{(SWIR1)}(551)$, $g^{(SWIR1)}(671)$, and $g^{(SWIR1)}(745)$, respectively. These VC gains were derived from the SWIR1-based VC approach using the VIIRS SWIR bands of 1238 and 1601 nm with $g^{(SWIR1)}(1238)$ and $g^{(SWIR1)}(1601)$ of 1.01812 and 0.994676, respectively. Note that with the SWIR-based VC approach, the gains for the NIR bands can also be derived. As described in Section 3.4, the SWIR gains of $g^{(SWIR1)}(1238)$ and $g^{(SWIR1)}(1601)$ are finalized after sufficient iterations in order to obtain the NIR VC gain $g^{(SWIR1)}(862)$ to converge to 1. Similar to the calculations of $g^{(NIR)}(\lambda)$ values, median values of the 21891 VC gain values are selected as the final VC gains for VIIRS mission-long ocean color data processing in order to filter out the anomalous $g^{(SWIR1)}(\lambda)$ values. The corresponding VC gains derived using the SWIR1-based VC approach for VIIRS bands along with the corresponding STD values are shown in Table 1.

Optics EXPRESS

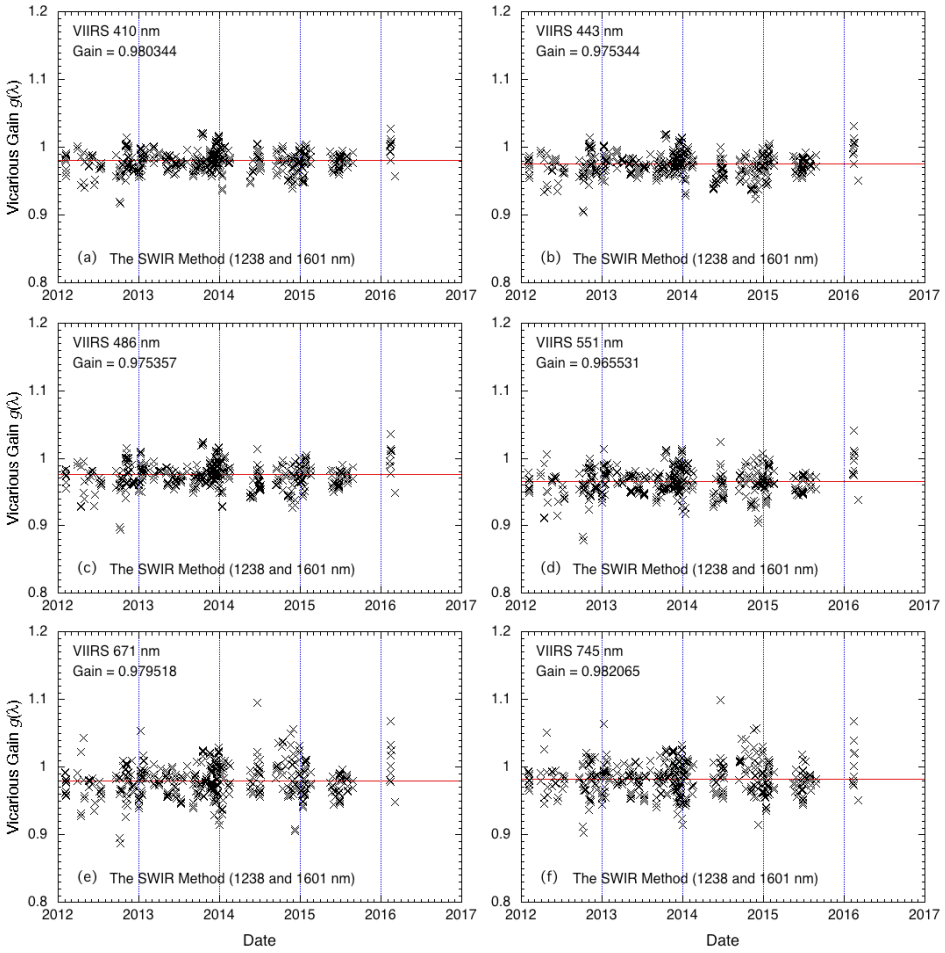

Fig. 3. VC gains $g^{(SWIR1)}(\lambda)$ as a function of time from 2012 to 2016 derived using the SWIR1-based VC method (with 1238 and 1601 nm bands) for VIIRS bands at (a) 410 nm, (b) 443 nm, (c) 486 nm, (d) 551 nm, (e) 671 nm, and (f) 745 nm. For a clear demonstration, $g^{(SWIR)}(\lambda)$ values are plotted in every 50 values for each plot.

Table 1. VIIRS-SNPP NIR- and SWIR-based vicarious gains.

VIIRS Band (nm)	NIR-Method		SWIR1-Method		SWIR2-Method		Difference (%)	
	Gains	STD	Gains	STD	Gains	STD	SWIR1 vs. NIR	SWIR2 vs. NIR
410 (M1)	0.979954	0.0129	0.980344	0.0190	0.980820	0.0181	0.040	0.088
443 (M2)	0.974892	0.0142	0.975344	0.0219	0.975609	0.0212	0.046	0.074
486 (M3)	0.974685	0.0131	0.975357	0.0246	0.975761	0.0240	0.069	0.110
551 (M4)	0.965832	0.0100	0.965531	0.0299	0.965888	0.0314	–0.031	0.006
671 (M5)	0.979042	0.0064	0.979518	0.0356	0.978576	0.0445	0.049	–0.048
745 (M6)	0.982065	—	0.982065	0.0379	0.981811	0.0476	0.000	–0.026
862 (M7)	1.00000	—	1.00001	0.0423	1.00000	0.0490	0.001	0.000
1238 (M8)	—	—	1.01812	—	1.01812	—	—	—
1601 (M10)	—	—	0.994676	—	—	—	—	—
2257 (M11)	—	—	—	—	1.20252	—	—	—

Optics EXPRESS

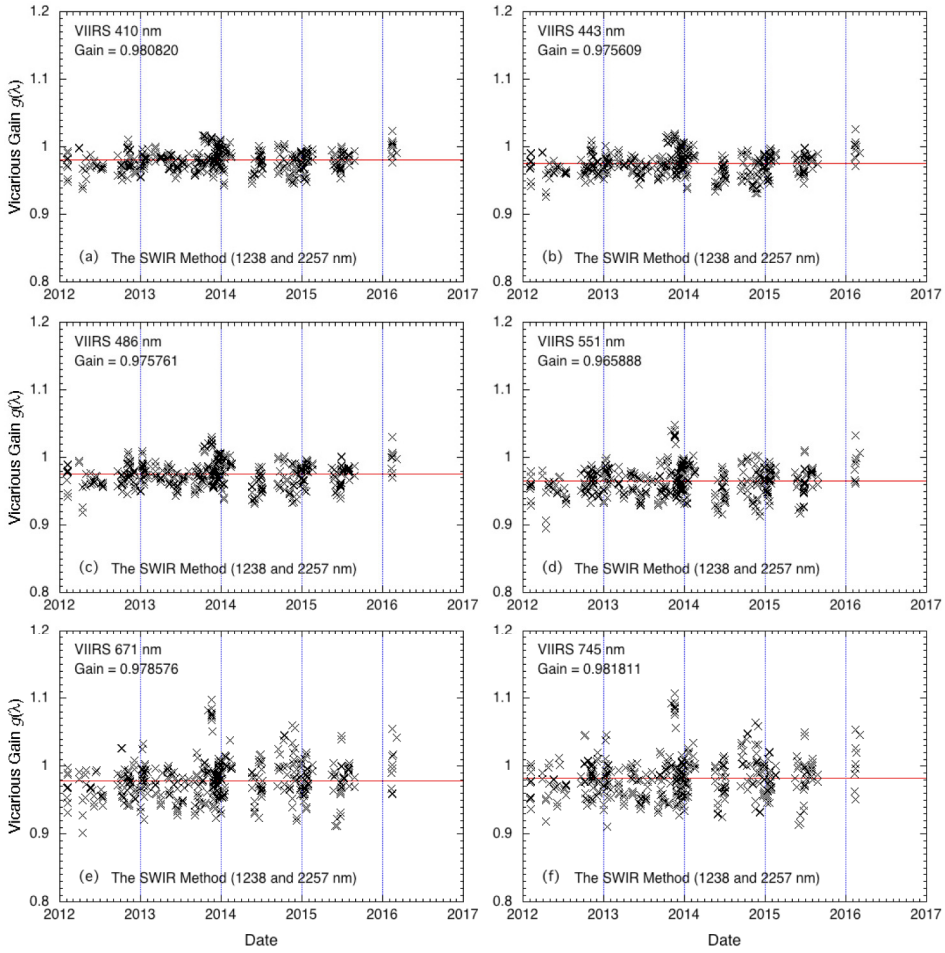

Fig. 4. VC gains $g^{(SWIR2)}(\lambda)$ as a function of time from 2012 to 2016 derived using the SWIR2-based VC method (with 1238 and 2257 nm bands) for VIIRS bands at (a) 410 nm, (b) 443 nm, (c) 486 nm, (d) 551 nm, (e) 671 nm, and (f) 745 nm. For a clear demonstration, $g^{(SWIR)}(\lambda)$ values are plotted in every 50 values for each plot.

Compared to results in Fig. 2 from the NIR-based VC method, the SWIR1-based $g^{(SWIR1)}(\lambda)$ results are noisier for all visible bands, and data noise actually increases with increasing wavelength (different from results in the NIR-based approach). For the NIR-based VC approach, atmospheric correction related data noise plays a much more important role than the noise from the sensor NIR band performance. In contrast, the sensor noises from the two SWIR bands [67] in the SWIR1-based ocean color data processing outweighed the noise due to imperfect atmospheric correction.

4.3. VIIRS-derived VC gains using the SWIR2-based approach

Figure 4 provides VIIRS gain results of $g^{(SWIR2)}(410)$ (Fig. 4(a)), $g^{(SWIR2)}(443)$ (Fig. 4(b)), $g^{(SWIR2)}(486)$ (Fig. 4(c)), $g^{(SWIR2)}(551)$ (Fig. 4(d)), $g^{(SWIR2)}(671)$ (Fig. 4(e)), and $g^{(SWIR2)}(745)$ (Fig. 4(f)), respectively, which were derived from the SWIR2-based VC approach using the SWIR bands 1238 and 2257 nm with $g^{(SWIR2)}(1238)$ and $g^{(SWIR2)}(2257)$ equal to 1.01812 and 1.20252, respectively. It should be noted that VC gains $g^{(SWIR2)}(1238)$ and $g^{(SWIR2)}(2257)$ were derived differently than VC gains $g^{(SWIR1)}(1238)$ and $g^{(SWIR1)}(1601)$. To derive $g^{(SWIR2)}(2257)$, $g^{(SWIR2)}(1238)$ was set to be the same as $g^{(SWIR1)}(1238)$, and the gain $g^{(SWIR2)}(2257)$ was computed by adjusting $g^{(SWIR2)}(2257)$ iteratively to achieve the goal for the gain of the VIIRS

Optics EXPRESS

NIR 862 nm band to be 1 at the MOBY site. When the gain $g^{(SWIR2)}(2257)$ is adjusted to 1.20252 (with $g^{(SWIR2)}(1238)$ of 1.01812), the NIR VC gain $g^{(SWIR2)}(862)$ reaches 1.00000. The VC gains for all visible bands (M1–M5) and the NIR 745 nm band (M6) can then be derived using the SWIR2-based VC approach with the VIIRS SWIR bands 1238 and 2257 nm. Therefore, $g^{(SWIR2)}(\lambda)$ for the VIIRS visible and NIR bands are derived separately from the VC approaches for deriving $g^{(SWIR1)}(\lambda)$ and $g^{(NIR)}(\lambda)$.

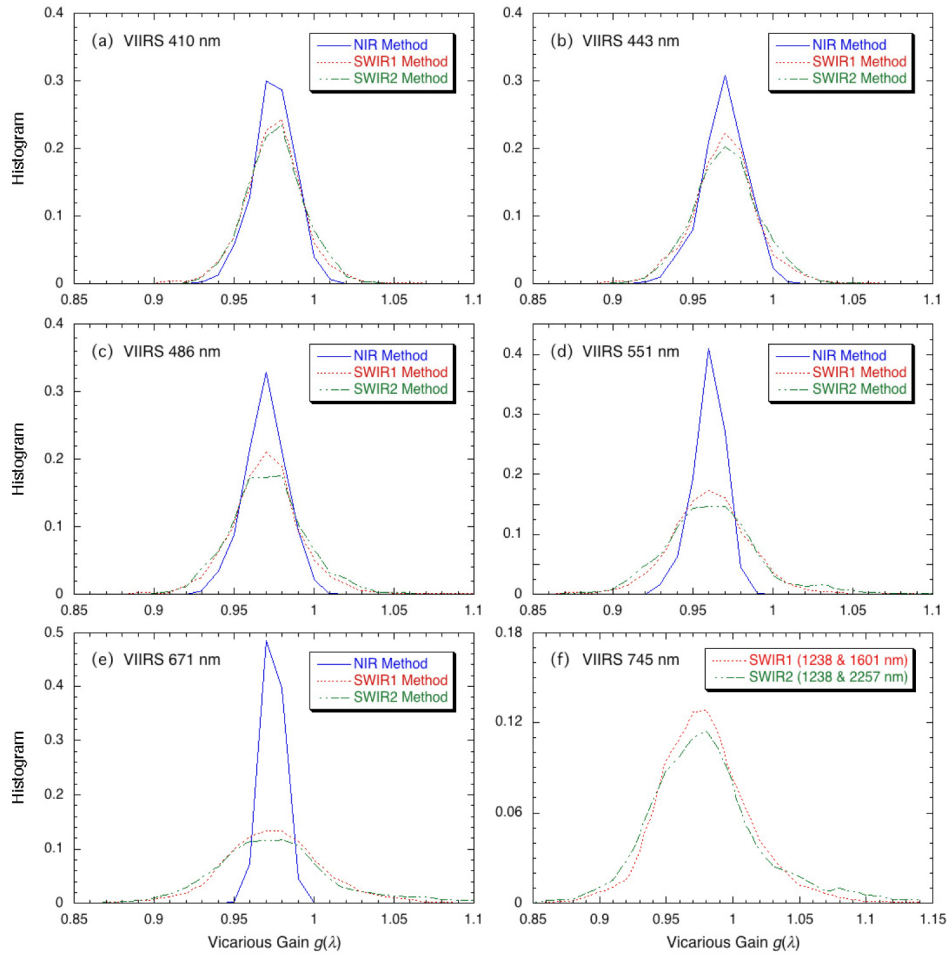

Fig. 5. Comparisons of histograms in the derived VC gains using the NIR-based, SWIR1-based, and SWIR2-based methods for VIIRS bands of (a) 410 nm, (b) 443 nm, (c) 486 nm, (d) 551 nm, and (e) 671 nm. Plot (f) shows histograms for the SWIR1-based VC gains $g^{(SWIR1)}(\lambda)$ and SWIR2-based VC gains $g^{(SWIR2)}(\lambda)$ at the VIIRS NIR 745 nm band (similar histogram distributions for the NIR 862 nm band).

Table 1 shows the VC gains using the SWIR2-based approach. Also shown in Table 1 are the corresponding STD values of the VC gains for the seven VIIRS M bands (visible and NIR bands). As expected, the $g^{(SWIR2)}(\lambda)$ noise, in terms of STD values, is comparable to the $g^{(SWIR1)}(\lambda)$ noise and larger than the noise for $g^{(NIR)}(\lambda)$.

4.4. Comparison of VIIRS-derived VC gains using the NIR- and SWIR-based approaches

Figure 5 compares histograms of $g^{(NIR)}(\lambda)$, $g^{(SWIR1)}(\lambda)$, and $g^{(SWIR2)}(\lambda)$ for VIIRS-SNPP bands at 410 nm (Fig. 5(a)), 443 nm (Fig. 5(b)), 486 nm (Fig. 5(c)), 551 nm (Fig. 5(d)), and 671 nm

Optics EXPRESS

(Fig. 5(e)). Figure 5(f) shows histograms of the VC gain distributions for the VIIRS NIR band $g^{(SWIR1)}(745)$ and $g^{(SWIR2)}(745)$ derived from the SWIR1-based and SWIR2-based VC methods. Histogram distributions for $g^{(SWIR1)}(862)$ and $g^{(SWIR2)}(862)$ are similar to those of $g^{(SWIR1)}(745)$ and $g^{(SWIR2)}(745)$. The histograms in Fig. 5 show that $g^{(NIR)}(\lambda)$, $g^{(SWIR1)}(\lambda)$, and $g^{(SWIR2)}(\lambda)$ have almost identical modes and median values even though the $g^{(SWIR1)}(\lambda)$ and $g^{(SWIR2)}(\lambda)$ results have wider distributions (larger STD values) than those from $g^{(NIR)}(\lambda)$ due to larger noise. As discussed previously, the $g^{(SWIR1)}(\lambda)$ and $g^{(SWIR2)}(\lambda)$ noise data are dominated by the VIIRS sensor noise at the SWIR bands, i.e., low signal-to-noise ratio (SNR) values [67]. For the NIR-based results, the width of the histogram (i.e., data noise or STD value) decreases with increasing wavelength, while for the SWIR-based VC approaches the width in distribution histograms (or STD value) increases with increasing wavelength. However, the NIR-based and two SWIR-based approaches show consistent vicarious gain results, i.e., VC gain factors $g^{(NIR)}(\lambda)$, $g^{(SWIR1)}(\lambda)$, and $g^{(SWIR2)}(\lambda)$ are almost identical for all visible bands (difference mostly within ~0.05%). In fact, the gain differences between the SWIR1- and NIR-based approaches for VIIRS bands at 410, 443, 486, 551, and 671 nm are 0.040%, 0.046%, 0.069%, –0.031%, and 0.049%, respectively (Table 1). The gain differences between the SWIR2 and NIR approaches for VIIRS bands at 410, 443, 486, 551, and 671 nm are 0.088%, 0.074%, 0.110%, 0.006%, and –0.048%, respectively (Table 1). It is also noted that differences of the $g^{(NIR)}(\lambda)$, $g^{(SWIR1)}(\lambda)$, and $g^{(SWIR2)}(\lambda)$ distributions (Fig. 5) are small in the shorter wavelengths such as at 410 nm (Fig. 5(a)) and 443 nm (Fig. 5(b)), and differences gradually increased with increasing wavelength in the green band of 551 nm (Fig. 5(d)) and the red band of 671 nm (Fig. 5(e)). As discussed previously, these large differences at the green and red bands between the NIR- and SWIR-based VC approaches are mainly caused by the poor sensor performance at the SWIR bands.

For $g^{(SWIR1)}(745)$ and $g^{(SWIR2)}(745)$ (Fig. 5(f)), and $g^{(SWIR1)}(862)$ and $g^{(SWIR2)}(862)$ (results not shown), the histograms are similar with close mode and STD values (Table 1). In particular, the two SWIR-derived NIR VC gains are consistent with the difference in VC gain in the NIR 745 nm equal to –0.026% (Table 1).

Table 2. Unified NIR and SWIR vicarious gains for VIIRS-SNPP.

VIIRS Spectral Band (nm)	Vicarious Gains
410 (M1)	0.979954
443 (M2)	0.974892
486 (M3)	0.974685
551 (M4)	0.965832
671 (M5)	0.979042
745 (M6)	0.982065
862 (M7)	1.00000
1238 (M8)	1.01812
1601 (M10)	0.994676
2257 (M11)	1.20252

The consistency of these VC gain results provides the fundamental basis for the ocean color data processing using the NIR-based, SWIR-based, and NIR-SWIR combined atmospheric correction algorithms for open oceans and turbid coastal/inland waters [8, 9, 55]. Therefore, a unified VC gain set can be used for the satellite ocean color data processing using the NIR- and SWIR-based ocean color data processing, which insures consistent ocean color products with different atmospheric correction algorithms (NIR, SWIR, and NIR-SWIR-based approaches). Table 2 provides the final unified VC gain set for VIIRS ocean color data processing. In the final VC gain set, $g^{(NIR)}(\lambda)$ values are used for $g(\lambda)$ in the VIIRS visible bands, i.e., $g(410)$, $g(443)$, $g(486)$, $g(551)$, and $g(671)$, to accurately derive ocean color products over global open oceans using the NIR-based atmospheric correction, while the

Optics EXPRESS

SWIR1-based VC gains are used for $g(745)$, $g(862)$, $g(1238)$, and $g(1601)$ and the SWIR2-based VC gain is used for $g(2257)$. It is noted that VC gains that keep four digits after the decimal point should be generally accurate enough for ocean color data processing.

With the unified VC gain set in Table 2, VIIRS mission-long ocean color data have been successfully reprocessed using the MSL12 with the NIR, SWIR, and NIR-SWIR methods. The VIIRS SWIR bands at 1238 and 1601 nm are used for the SWIR-based approaches for the ocean color data processing. VIIRS mission-long reprocessed ocean color images using the NIR-based, SWIR-based, and NIR-SWIR combined approaches and extensive calibration and validation results can be found at: (www.star.nesdis.noaa.gov/sod/mecb/color/).

5. Discussions and summary

The sensor on-orbit vicarious calibration is a key calibration procedure necessary for satellite ocean color remote sensing. The VC methodology outlined by *Gordon* (1998) [44] and used for various satellite ocean color sensors, e.g., SeaWiFS, MODIS, MERIS, VIIRS, is really a relative spectral VC approach utilizing the power of Rayleigh scattering. It has been shown that, in order to fully use the power of Rayleigh scattering, the on-orbit VC for ocean color data processing should be carried out from *the longer wavelength to the shorter wavelengths*. With such an approach, sensor calibration errors after VC can be significantly reduced. Therefore, accurate ocean color products can be derived using the vicariously calibrated TOA radiance spectra data.

Even though satellite ocean color products have been routinely produced using the NIR-based data processing approach for the global ocean (e.g., from SeaWiFS, MODIS, MERIS, VIIRS), the NIR atmospheric correction can lead to significant errors in $nL_w(\lambda)$ spectra over turbid coastal and inland waters. It has been shown that the SWIR-based and NIR-SWIR combined atmospheric correction approaches in the ocean color data processing are useful to derive accurate ocean color products over turbid coastal and inland waters. Thus, it is necessary to have a VC approach that derives consistent VC gain set for the ocean color data processing using the NIR-, SWIR-, and NIR-SWIR-based atmospheric correction algorithms.

In this study, we developed a VC approach for deriving consistent vicarious gains for the NIR- and SWIR-based ocean color data processing. Specifically, using the in situ MOBY optics observations between 2012 and 2016, VC gain coefficients for VIIRS-SNPP with the NIR and SWIR VC approaches are derived. There are a total of 21891 valid $g(\lambda)$ values for VIIRS VC over the MOBY site. This pixel-based methodology is used to compute VC gains in the MOBY site, and no aerosol model is assumed in order to derive $g^{(NIR)}(\lambda)$ for the shorter NIR wavelengths (i.e., 745 nm for VIIRS). No arbitrary outlier filter for $g(\lambda)$ is necessary with the proposed VC methodology and it is particularly more effective to deal with the noisy $g(\lambda)$ coefficient in the SWIR-based calibration. The histograms of the derived $g(\lambda)$ are generally normal distributions, suggesting that $g(\lambda)$ from the proposed methodology is close to the mode values of the $g^{(NIR)}(\lambda)$, and the impact of the noise on $g^{(SWIR1)}(\lambda)$ and $g^{(SWIR2)}(\lambda)$ is minimized when median $g(\lambda)$ values are derived. It should be noted that the VC gains are different for different SDR (or Level-1B) data and different ocean color data processing algorithms (or associated Rayleigh and aerosols lookup tables). In particular, accurate on-orbit instrument calibration and specifically for characterizing sensor on-orbit degradation trend precisely over time are critical to derive reliable VC gains for applications of satellite ocean color remote sensing [43].

We show that the NIR- and SWIR-based VC approaches, i.e., $g^{(NIR)}(\lambda)$, $g^{(SWIR1)}(\lambda)$, and $g^{(SWIR2)}(\lambda)$ values, are consistent with a discrepancy mostly within ~0.05% for VIIRS-SNPP, providing the foundation for the ocean color data processing with different approaches. A unified VC gain set for VIIRS-SNPP ocean color data processing has been derived and implemented in the MSL12. Therefore, using the unified VC gain set, the VIIRS mission-long ocean color products have been successfully reprocessed using the MSL12 with the NIR, SWIR, and NIR-SWIR combined methods. These three VIIRS ocean color product data

Optics EXPRESS

streams (i.e., NIR-, SWIR-, and NIR-SWIR-based approaches) are currently going forward using the MSL12 with the same unified gain set shown in Table 2.

Acknowledgments

This work was supported by the Joint Polar Satellite System (JPSS) funding. The authors are grateful to the MOBY team for providing the in situ data in support of various satellite ocean color missions. The views, opinions, and findings contained in this paper are those of the authors and should not be construed as an official NOAA or U.S. Government position, policy, or decision.